Theoretical and Applied Climatology (2021) 144:239–252
https://doi.org/10.1007/s00704-021-03518-y

ORIGINAL PAPER

Impacts of low cloud and fog on surface radiation fluxes for ecosystems in coastal California

Andrew J. Oliphant[1] · Sara A. Baguskas[1] · Daniel M. Fernandez[2]

Received: 24 May 2020 / Accepted: 4 January 2021 / Published online: 31 January 2021

Abstract

Advection fog processes produce frequent low cloud and fog (LCF) during summer along the coast of central and northern California. Four radiometer datasets from sites in San Francisco and Monterey Bay as well as fog-drip and meteorological observations were used to characterize the role of LCF on surface radiation budget components and scattering of solar radiation. LCF produced distinct and consistent impacts on surface radiation relative to clear skies including large reductions (approximately half) in solar irradiance but large increases (approximately 180%) in the diffuse beam component, consistent increases of approximately 70 W m^{-2} in down-welling longwave radiation ($L\downarrow$), as well as reductions in net radiation and leaf surface temperature by day and increases at night. $L\downarrow$ can be a useful and accurate tool for monitoring the presence of LCF, using simple thresholds: LCF = $L\downarrow > 360$ W m^{-2} and clear-sky = $L\downarrow <$ 340 W m^{-2}. Based on this, LCF conditions prevailed 60% of hours during summer, peaking consistently at 08:00 PDT, with clear skies occurring 33% and mixed conditions 7% of hours. The ratio of the incident surface to extraterrestrial solar radiation (τ) is also useful to determine LCF presence during daylight hours, using LCF = $\tau < 0.0059\beta + 0.3$ and clear-sky = $\tau > 0.0059\beta + 0.3$, where β is the solar elevation angle. We also present a model to partition the diffuse and direct beam fractions of solar irradiance specifically for coastal LCF, which improved accuracy by more than 10% relative to existing universal models. These radiation characteristics are important for understanding energy balance and sunlight conditions experienced by coastal ecosystems.

Keywords Surface radiation budget · Advection fog · Microclimate · Coastal California

1 Introduction

Low cloud and fog, along with cool onshore flow, dominate the coastal climate of central and northern California during summer months (Pilié et al. 1979; Leipper 1994; Null 1995). The persistent summertime synoptic weather pattern is dominated by the North Pacific High centered off the coast of California, which inhibits the presence of deeper convective and frontal clouds. However, the cold California Current and coastal upwelling, combined with onshore flow, produce an advection fog that is persistent in summer months (Leipper 1994). Onshore (predominantly northwest) winds are generated by a combination of the synoptic scale North Pacific High and a regional-scale sea breeze system produced by strong temperature gradients across the coastline (Null 1995). The spatiotemporal cloud coverage has been well documented from space (Jensen et al. 2008; Clemesha et al. 2016; Torregrosa et al. 2016) and tends to form over the eastern Pacific Ocean in the vicinity of the central and northern Californian coast and extend inland due to onshore airflow (Pilié et al. 1979; Null 1995). The inland extent of the marine layer clouds is typically on the order of kilometers to tens of kilometers and has a maximum extent during the night and early morning, often dissipating during the warmer part of the day (Jensen et al. 2008; Iacobellis and Cayan 2013; Clemesha et al. 2016; Torregrosa et al. 2016). The latter study showed that, for most of coastal California, high and deep clouds occurred for less than 48 h in total between June and September, while fog and low cloud cover dominated the region, with many locations receiving more than 14 h per day over the same period.

Fog has been variously defined as a cloud in contact with the ground or water droplets near the surface producing visibility of less than 1 km (Leipper 1994). The marine stratus and stratocumulus clouds that dominate coastal California during the dry Mediterranean climate summer are sometimes fog by

✉ Andrew J. Oliphant
andrewo@sfsu.edu

[1] Department of Geography & Environment, San Francisco State University, San Francisco, CA, USA

[2] Department of Applied Environmental Science, California State University Monterey Bay, Seaside, CA, USA

definition, but often more strictly low-level clouds with bases lower than 2 km and more commonly within a few hundred meters of the surface (Pilié et al. 1979). In addition, the same cloud bank might be defined as low-level stratus or stratocumulus at the coastline and fog a short distance inland where the cloud makes contact with upland areas of the Coast Range that runs parallel with the coast. For example, a recent study showed much higher levels of fog deposition occurring in inland hills than in adjacent coastal locations (Weiss-Penzias et al. 2016). Locally these variants of coastal cloud conditions are collectively and colloquially known as "fog." Here we use the acronym "LCF" to characterize the low clouds or fog that dominate the cloud climatology of coastal California during summer.

The narrow coastal band of LCF influence in California, often referred to as the "fog belt," supports unique terrestrial biodiversity (Mooney et al. 2001; Vasey et al. 2014) and economically-important agriculture (Baguskas et al. 2018). The most well-studied impacts of LCF on coastal plant communities is related to reduction of summer drought stress through fog water deposition (Dawson 1998; Corbin et al. 2005; Hiatt et al. 2012; Carbone et al. 2013; Iacobellis and Cayan 2013; Weiss-Penzias et al. 2016), reduced plant water stress and transpiration (Fischer et al. 2009; Vasey et al. 2012; Baguskas et al. 2014), as well as enhanced water use efficiency (Baguskas et al. 2018). Other climate impacts of coastal fog include the role of shade (Carbone et al. 2013) and air temperature (Iacobellis and Cayan 2013), which produce a cooling effect by day and warming at night. Relatively little has been published on the microclimate controls of fog on coastal ecosystems, particularly the surface radiation budget, which is important for plant energy balance and light availability for photosynthesis.

The primary focus of this research is to characterize the impact of LCF on the surface radiation regime in coastal California, particularly those radiation fluxes important to ecosystem functioning. In addition, challenges remain for continuous monitoring of LCF presence, which is principally achieved from satellite observations from above (Torregrosa et al. 2016; Clemesha et al. 2016); surface-mounted lidar or sodar systems, and visibility and radiosonde records from coastal airports (which are often sited to avoid foggy environments) (Williams et al. 2008) or the combination of satellite-derived imagery and ground observations (Rastogi et al. 2016). Therefore, a secondary objective of this study is to determine whether surface-mounted radiometers can be useful for monitoring the presence of fog and characterizing temporal frequency at the local scale.

2 Theoretical background and methods

Clouds and other atmospheric aerosols alter the magnitude of each of the surface radiation budget (SRB) components,

$$Q^* = K^* + L^* = (K\downarrow - K\uparrow) + (L\downarrow - L\uparrow) \quad (1)$$

where Q, K, and L represent all-wave, shortwave (solar spectrum), and longwave (thermal infrared) radiation, respectively, while arrows represent the direction of the radiant flux, and * denotes the net balance between down-welling and upwelling radiation. Net radiation (Q^*) reflects the balance of the four independent flux components and is the major driver of the surface energy balance from the leaf to ecosystem scale. An additional radiant flux assessed in this study is photosynthetically active radiation (PAR), which is a subset of the solar spectrum (0.4–0.7 μm) that is used by plants for photosynthesis.

2.1 Fog impacts on solar radiation

In general, clouds have been shown to reduce the quantity of $K\downarrow$ reaching the surface due to absorption within and upward reflection from the cloud. The total reduction in atmospheric transmissivity (τ), often referred to as the clearness index (e.g., Gu et al. 1999), can be simply defined by,

$$\tau = \frac{K\downarrow}{K_{Ex}} \quad (2)$$

where K_{Ex} is solar radiation at the top of the atmosphere, which can be modeled given geographic location and time of day and year (e.g., Whiteman and Allwine 1986). In addition, multipath scattering by refraction through cloud droplets enhance the portion of solar radiation arriving at the surface in diffuse beam form, which is approximately isotropic in direction, relative to the direct beam from the solar position (Aida 1977).

The reduction in $K\downarrow$ is unlikely to impact the surface albedo (α) significantly because albedo is primarily a function of surface properties; however, it directly reduces $K\uparrow$, since $K\uparrow = \alpha.K\downarrow$. Albedo itself is governed in part by the sun angle and so should have a smaller diurnal range under fog (approximately isotropic irradiance) versus clear sky (strongly sun angle-dependent irradiance).

Since PAR dominates the peak of the solar emission spectrum, reduction of total or global PAR (PAR_G) also occurs in the presence of clouds. Analogous to the full solar spectrum, PAR_G is comprised of both direct beam (PAR_S) and diffuse beam (PAR_D) forms of irradiance, whereby $PAR_G = PAR_S + PAR_D$. PAR_D is likely to be enhanced and PAR_S diminished beneath LCF, due to the alteration of radiant path directions, as with other clouds. This is important to characterize because the light use efficiency of PAR_D has been shown to be significantly higher than PAR_S for most plant communities (e.g., Gu et al. 1999; Alton 2008; Oliphant et al. 2011; Hemes et al. 2020). The relative proportion of PAR arriving in diffuse beam form (ϕ) can be defined by

$$\phi = \frac{PAR_D}{PAR_G} \quad (3)$$

It has been widely shown that there is a fairly consistent negative relationship between τ and ϕ, such that PAR_D can be modeled using only observations of $K\downarrow$ (e.g., Erbs et al. 1982; Weiss and Norman 1985; Reindl et al. 1990; Roderick (1999). A recent evaluation of these models using a global dataset of radiation observations yielded a universal equation with reasonable accuracy (Oliphant and Stoy 2018). However, the evaluation also showed that variations in model coefficients existed among sites due primarily to differences in sky conditions, (e.g., atmospheric aerosol concentrations and cloud types and depths) and that local model training could improve accuracy significantly. Therefore, it will be useful to refine the model for areas dominated by LCF.

2.2 Fog impacts on the longwave radiation budget

Clouds impact both emissivity and temperature of the overlying atmosphere and therefore the magnitude of $L\downarrow$. During the conditions that produce coastal LCF in California, air temperatures are typically in the range of 10–15 °C. Thus, the impact fog has on $L\downarrow$ can be approximated using the Stefan-Boltzmann law,

$$L\downarrow = \varepsilon\sigma T^4 \tag{4}$$

where ε is emissivity, σ is the Boltzmann constant (5.67×10^{-8}), and T is temperature (K) of the emitting objects (gasses, aerosols, and droplets). In the case of LCF presence, assuming an emissivity of 0.99 based on the emissivity for water clouds of 100 m thick or more (e.g., Chylek and Ramaswamy 1982) and cloud base temperatures close to air temperatures (~10–15 °C), down-welling longwave radiation would likely range from approximately 360 to 385 W m^{-2}. The emissivity of clear skies (ε_{cs}) varies most strongly as a function of atmospheric column vapor pressure (e_a), and Staley and Jurica (1972) provided a simple empirical model to parameterize it,

$$\varepsilon_{cs} = Ce_a{}^m \tag{5}$$

where C is 0.67 and m is 0.08. Based on a range of e_a values of 10–13 hPa observed at a coastal site in Monterey Bay during summer months, ε_{cs} would range from about 0.81 to 0.82. Using these emissivity values and a temperature range of 10–20 °C, the range in $L\downarrow$ during periods of clear skies would be approximately 295–340 W m^{-2}. Thus, the populations of $L\downarrow$ under clear sky versus LCF are likely to be quite different from one another.

2.3 Observational dataset

The dataset used for this analysis was generated from four micrometeorology deployments in the north and central coast of California (Fig. 1), providing six summers of 15- or 30-min average radiation data over the span of 12 years (Table 1). The four sites included (1) the living roof of the California Academy of Sciences building in San Francisco (SFCAS), (2) the astronomical observation deck on top of Thornton Hall, San Francisco State University (SFSU), (3) a coastal strawberry farm in northern Monterey Bay (MBCF), and (4) Fritzsche Field airfield located inland from southern Monterey Bay (MBFF). From each dataset, radiation data from the months of June, July, and August were extracted to represent the main period of advection fog occurrence. In each case, two bandwidths of radiation were measured in opposite vertical directions using high accuracy pyranometers and pyrgeometers: CNR1, Kipp & Zonen, Delft, The Netherlands, and NR01, Hukseflux, Delft, The Netherlands (Table 1). When unobstructed by surface features, these measure the down-welling and upwelling components of short and longwave radiation independently and allow calculation of Q^* using Eq. 1. In addition, on two of the deployments (SFCAS and SFSU), a BF3 or BF5 diffuse PAR sensor was deployed (Delta-T, Cambridge, UK), which measures both PAR_G and PAR_D directly, from which ϕ was calculated using Eq. 3. Fog-drip was measured at two of the sites (MBCF and MBFF) using a 1.00 m^2 mesh passive collector and tipping bucket rain gauge, as described in Fernandez et al. (2018).

For each study site, K_{Ex} was modeled for each time-step of the radiation observations using the method described in Oliphant et al. (2003). Following this, τ was calculated using Eq. 2, with $K\downarrow$ provided by the upward-pointing pyranometer deployed there. Surface temperature ($T_{surface}$) was estimated from a rearrangement of Eq. 4 such that,

$$T_{surface} = \left[\frac{L\uparrow}{\varepsilon_s\sigma}\right]^{0.25} \tag{6}$$

where ε_s is the surface emissivity. For our cases, we used ε_s = 0.97 for the vegetated surfaces at SFCAS, MBCF, and MBFF after Rubio et al. (1997), and for SFSU, where the surface was predominantly a mix of concrete and asphalt, we used 0.92 after Yang et al. (2015).

2.4 Instrument and measurement uncertainties

The radiometers we used are generally well regarded and widely used within the micro- and bio-meteorological research communities (e.g., Brotzge and Duchon 2000, Blonquist et al. 2009, Emmel et al. 2020). Each of our net radiometers and PAR sensors were sent back once for factory recalibration over the timespan of this study. We also performed our own comparison between the two sets of radiometers in May 2016. Instruments were co-located on the SFSU rooftop site for 1 week collecting 30-min averages and included periods of both LCF and clear sky conditions. Although this comparison had no traceable reference for absolute accuracy estimation, it provides a measure of comparability of instruments used at different sites in this study.

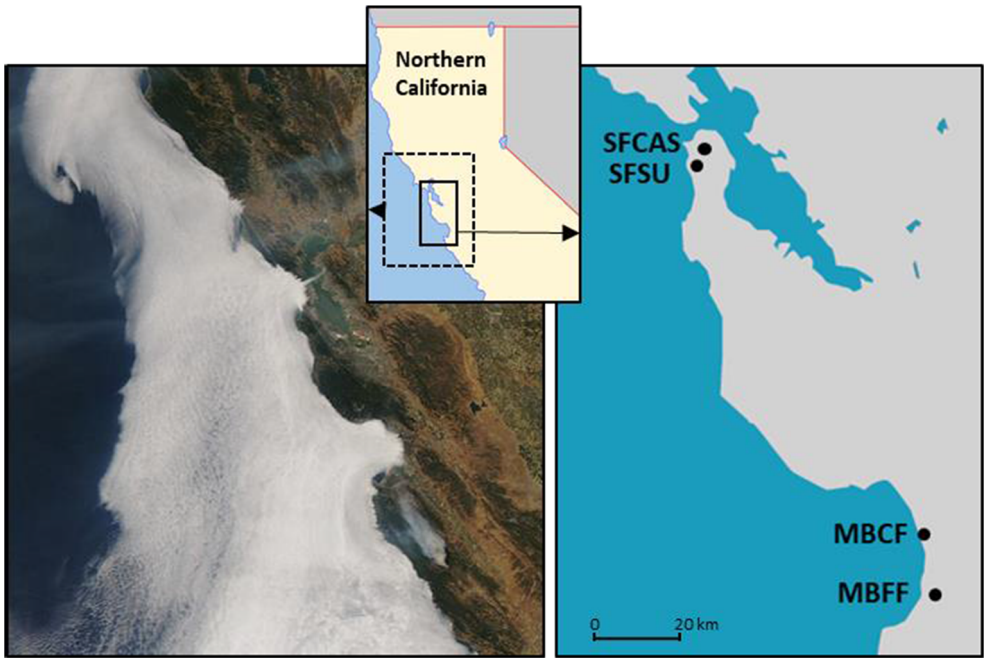

Fig. 1 Satellite image (left) showing typical summer LCF along the central Californian coast (image captured July 2008, source NOAA), site map (right) showing location of observation sites in San Francisco (SF) and Monterey Bay (MB) and location map (inset) of central and northern California

Factory calibrations for both of the net radiometers used in this study showed errors less than 5% with slightly higher error for the pyrgeometers than pyranometers. Comparison between factory calibrations showed drift on the order of 1% per year. In a comparison of a range of commonly used net radiometers, Blonquist et al. (2009) found that both the CNR1 and NR01 performed among the most accurately (relative to a reference sensor), with differences around 2% for pyranometers and 5% for pyrgeometers. We also found close agreement between the two radiometers used, based on our 2016 intercomparison. The mean absolute differences between the sensors ranged from 2.49 W m^{-2} for $L\downarrow$ to 7.13 W m^{-2} for Q^*. As a percentage of the average magnitudes observed for each radiation component, they ranged from 0.7% for $L\downarrow$ to 6.1% for $K\uparrow$.

Neither of the net radiometers were aerated or heated to remove droplets from the domes during fog events. This can impact refraction of shortwave and emission of longwave radiation detected by the radiometers (Brotzge and Duchon 2000). Bradley and Gibson (1982) concluded from aircraft studies in clouds that the pyrgeometer with droplets underestimated longwave radiation observed, although these were negligible near the base of the cloud. Brotzge and Duchon (2000) found small differences in net radiation (maximum of 15 W m^{-2}) between aerated and non-areated radiometers during rain events. We compared nocturnal $L\downarrow$ values under LCF conditions with and without fog-drip occurrence. We used high values of $L\downarrow$ at night (> 360 W m^{-2}, see Section 2.2) to limit data to likely LCF conditions and the passive fog collector to distinguish fog deposition conditions from "dry" LCF conditions. $L\downarrow$ averaged 3.6 W m^{-2} lower during fog-drip conditions than during dry conditions ($p < 0.001$ at 95% confidence level) which may be related to the deposition of droplets on the radiometer dome.

The Delta-T BF3 and BF5 PAR sensors are well tested and widely used by the biometeorological community (e.g.,

Table 1 Site characteristics and experimental details for four radiometer deployments along the central and northern coast of California, USA

Site general location	Site name	Elev. (masl)	Lat. (°N) Lon (°W)	Distance inland	Observation periods	Freq. (min)	Radiometers deployed
Central San Francisco	SFCAS	87	37.7699 122.4655	4.3 km	2014 Jun–Jul 2015 Jun–Aug	30	HukseFlux NR01, Delta-T BF5
Southwest San Francisco	SFSU	79	37.7242 122.4771	2.6 km	2005 Jun–Aug 2006 Jun–Aug	15	Kipp & Zonen CNR1, Delta-T BF3
Monterey Bay Coastal Farm	MBCF	21	36.8477 121.7894	1.6 km	2016 Jun–Aug	30	Kipp & Zonen CNR1
Fritzsche Field Airfield, MB	MBFF	48	36.6955 121.7575	4.7 km	2015 Jul–Aug	30	HukseFlux NR01

Emmel et al. 2020). The main advantage is their ability to directly determine the ratio of diffuse to total PAR without moving parts. Seven cosine-corrected photodiodes are arranged under a patterned, hemispherical dome presenting at least some of the photodiodes in direct line with the sun and some shaded by the patterned dome for any time of day or year. The overall accuracy for the PAR and PAR_D measurements, as reported in their specification sheets, is rated at ± 10 μmol m^{-2} s^{-1} for both the BF3 and BF5 sensors. The spectral response of the BF3 and BF5 are a little different to each other and with a higher response in the blue part of the spectrum for the BF3 than BF5 sensor, although both are factory calibrated to the ideal PAR response. We found close agreement between the two sensors used in this study based on the intercomparison conducted in May 2016, when the mean absolute differences between the two sensors were 4.29 μmol m^{-2} s^{-1} (0.5%) for PAR and 3.16 μmol m^{-2} s^{-1} (0.7%) for PAR_D, and differences scaled closely with the magnitude of PAR ($r^2 > 0.98$). Because differences were small and instruments were recalibrated at different times during the study prior to the intercomparison and the rate of drift is unknown, we chose not to correct data based on the differences determined in the intercomparison.

3 Results

3.1 Signatures of fog presence in surface radiation components and derivatives

The surface radiation characteristics of a period of 10 days (DOY 176–186 in 2016) in MBCF is shown in Fig. 2. When fog-drip occurred, three immediate and consistent radiometric responses emerged. The first was a sharp increase in $L\downarrow$ from approximately 300 to 370 W m^{-2} that was synchronous with fog-dripdetection. The other two responses are apparent only during daylight hours, including a decrease in $K\downarrow$ relative to K_{Ex} and an increase in PAR_D relative to PAR_G. Based on these radiometric response characteristics, it is also evident that there were periods when the radiometric response indicated fog conditions, while no fog-drip was recorded (e.g., days 182–185 in Fig. 2). Over this period, the relative humidity ranged between 80 and 95%, suggesting that cloud cover was not in contact with the surface.

During the day, the reduction in $K\downarrow$ under LCF conditions also reduced $L\uparrow$, further enhancing L^*, although this gain was smaller than the reduction in K^*, resulting in a net decrease in Q^* (e.g., day 182, Fig. 2). In general, LCF resulted in a much smaller net longwave radiative loss at night indicated by the departure between $L\downarrow$ and $L\uparrow$ (e.g., the early hours of day 183, Fig. 2). Because the California coastal advection fog frequency is greatest at night, the presence of fog over the diurnal cycle may go undetected by solar observations (e.g., days 176 and 179, Fig. 2). In contrast, because of its diurnally consistent response, and the fact that it is very rare for other clouds to form over coastal California in summer, a simple $L\downarrow$ threshold may produce a better way to detect the presence of LCF. In the next two sections, we examine longwave and shortwave impacts of LCF in more detail, before providing a radiation climatology for the California coastal summertime under both clear sky and LCF conditions.

3.2 LCF impacts on longwave radiation

Summertime frequency distributions of $L\downarrow$ from the four sites are compared in Fig. 3. These show similar bimodal distributions at all sites, with modes focused near 310 and 375 W m^{-2}, and a minimum between the two modes at around 350 W m^{-2}. The narrower, higher mode reflects the fairly consistent cloud base temperature under foggy conditions (typically about 10–15 °C). This is because the range of cloud base heights during advection fog conditions is fairly small, typically less than 1000 m, and the meteorological conditions that produce LCF are quite distinct and consistent throughout the summer months. The lower mode (approx. 280–340 W m^{-2}) reflects the population of clear sky periods, and the distribution is significantly wider than the foggy mode. This is likely due to the greater variability of lower tropospheric temperatures experienced under "clear sky" conditions, which can range from onshore marine flow with temperatures similar to LCF periods to easterly flows bringing relatively warm, dry continental air masses (Null 1995).

At the SFSU site, a total of 490 visual observations of sky conditions were made on campus at intermittent intervals over two summers of the radiation deployments, distinguishing three sky categories; complete LCF cover (269 observations), clear sky (172 observations), or partial LCF cover or other clouds (49 observations). $L\downarrow$ was found to be greater than 360 W m^{-2} for 97% of observations that reported "overcast," and $L\downarrow$ was less than 340 W m^{-2} for 95% of "clear sky observations". The third, much smaller, category of "mixed sky" mostly resulted in $L\downarrow$ between 340 and 360 W m^{-2} for 59% of observations from the visual record, with 26% falling in the "overcast," and 15% in "clear sky" conditions. At the Monterey Bay sites, which included fog deposition measurements, $L\downarrow$ was greater than 350 W m^{-2} on 95% of periods that also recorded fog-drip at MBCF (which averaged 370 W m^{-2}) and 97% of periods at MBFF (which averaged 374 W m^{-2}).

Based on the $L\downarrow$ values found under different sky conditions from visual observations and the minima between the two modes in the $L\downarrow$ frequency distributions (Fig. 3), the simple $L\downarrow$ threshold of 350 W m^{-2} to identify fog or low cloud presence in the summer records may be the most useful signal, whereby LCF conditions are defined by $L\downarrow > 350$ W m^{-2}, and clear sky conditions are defined by $L\downarrow < 350$ W m^{-2}. However, when dealing with 30-min or hourly averages of

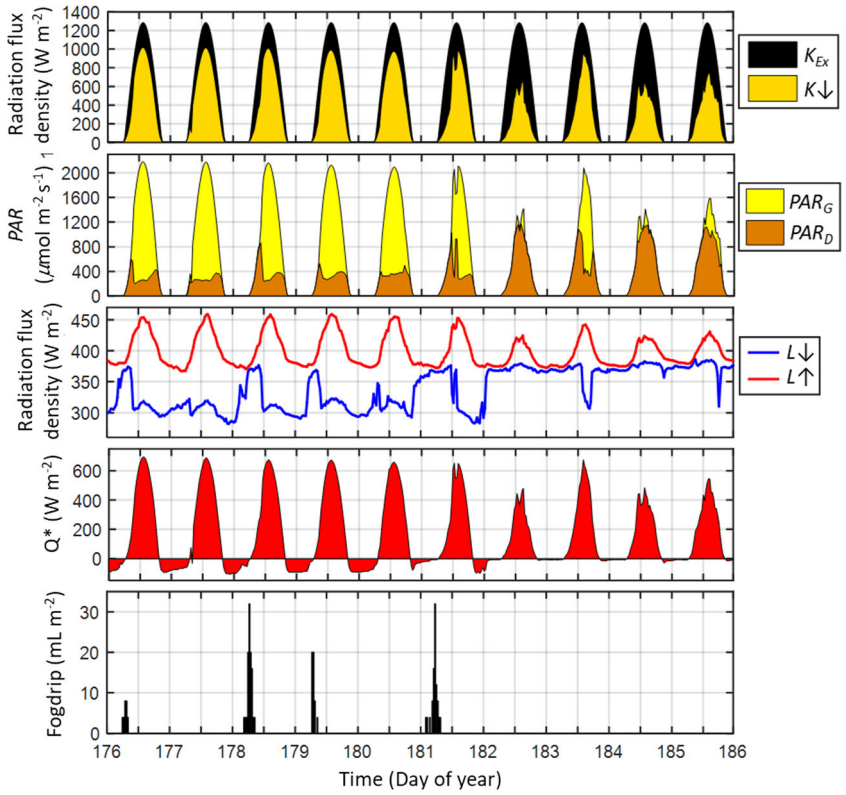

Fig. 2 Time series of 30-min average radiation budget components and fog-drip at MBCF over 10 days (June 24 to July 3, 2016) to illustrate the range of summer sky conditions observed

1-Hz samples, some confusion can be found in intermediate values (around 350 W m^{-2}). Although infrequent (Fig. 3), these intermediate values potentially include both mixed clear and cloudy skies occurring during the averaging period, which typically occur during both the onset and dissipation of LCF

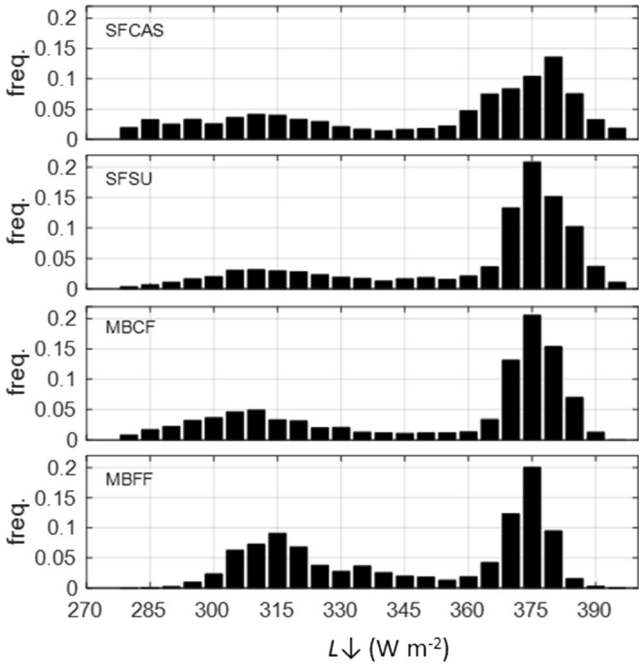

Fig. 3 Frequency distributions of $L\downarrow$ for summertime (June–August) 30-min average periods

events, and the rarer cases of persistent (within the averaging period) but cooler (higher) clouds. For this reason, it is helpful to include standard deviations in data logger averaging periods. In this case, relatively high standard deviation (~20 W m^{-2}) is indicative of a strong bimodal signal (mixed LCF and clear skies), while much smaller standard deviation (~2 W m^{-2}) results from persistent higher clouds. Most of our samples were in the higher category of standard deviation suggesting that they included mixed LCF and clear skies and indicating the very bimodal cloud climatology at these sites in summer months. In order to include mixed skies in the definition of sky conditions, double thresholds are recommended, whereby LCF conditions are defined by $L\downarrow > 360$ W m^{-2}, clear sky conditions are defined by $L\downarrow < 340$ W m^{-2}, and mixed skies are represented by $340 <= L\downarrow <= 360$ W m^{-2}.

We also attempted to distinguish the difference between fog and low cloud from the radiometric record, using non-zero fog-drip records to define the presence of fog. For each 30-min period defined as LCF (i.e., $L\downarrow > 360$ W m^{-2}), we calculated the departure between air temperature (T_a) measured at 3 m above ground level and cloud base temperature (T_c). T_c was calculated from $L\downarrow$ by rearranging the Stefan-Boltzmann Law as in Eq. 6 and using a water cloud emissivity of 0.99. All of the periods when fog-drip was recorded (8% of all LCF records) had a temperature departure of less than 2 °C. However, a further 87% of LCF records also had a temperature departure of less than 2 °C but did not result in fog-drip. The remaining 5% of data determined that LCF did not result

in fog-drip and had a temperature departure greater than 2 °C (up to a maximum of 5.5 °C). While we have also observed fog that did not result in fog-drip, we conclude from this exercise that we were not able to distinguish fog from low clouds successfully using this method.

3.3 LCF impacts on shortwave radiation

Because of the high solar angle-dependence of $K\downarrow$, and the large impact LCF has on both reducing $K\downarrow$ and increasing the scattered portion, the transmission fraction (τ, Eq. 2) and diffuse PAR fraction (ϕ, Eq. 3) are useful indicators of the presence of LCF during daylight hours. This is particularly the case in coastal California, because the occurrence of clouds other than those produced by advection fog are extremely rare in summer. The distribution of τ during summer at all four sites is provided in Fig. 4. The narrower peak in the distribution (between 0.7 and 0.8) occurs when atmospheric transmission is at its greatest, suggesting the absence of clouds, while the much wider distribution peaking at about 0.25 is suggestive of LCF presence due to the large reduction in radiation reaching the surface. The τ value at the distribution minimum between the two modes ranged between 0.55 and 0.65 among sites. From the visual sky condition record at SFSU, τ was less than 0.6 on 87% of periods when "overcast" was reported, and τ was greater than 0.6 for 83% of periods when "clear sky" was reported. At the two sites that measured fog deposition, the average τ during daylight periods when fog deposition was recorded was 0.32 ± 0.15 at MBCF and 0.39 ± 0.19 at MBFF.

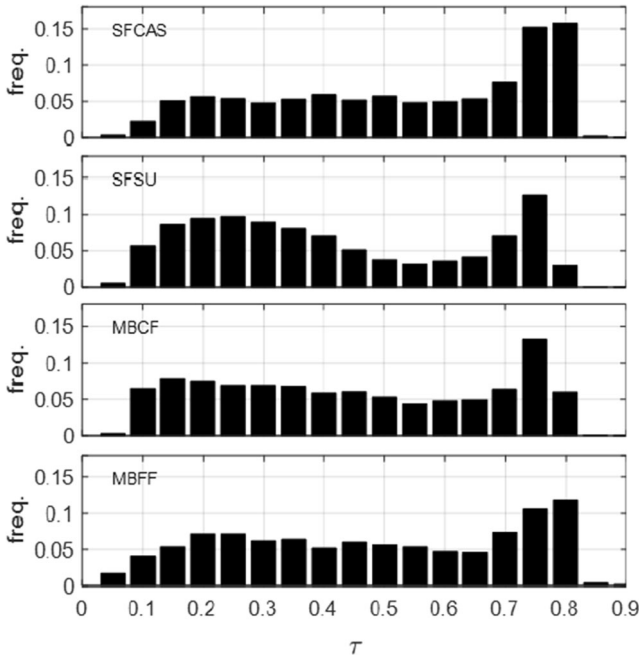

Fig. 4 Frequency distribution of τ for the four study sites, using data from June–August

The large variability in τ for LCF compared with clear sky conditions is probably related to variation in optical depth of clouds, due to both differences in cloud density and depth and differences in optical path-length associated with solar zenith angle.

The diffuse fraction (ϕ) was also strongly bimodal, with the high mode reflective of the very high degree of scattering that occurs beneath most clouds and the narrowness of the mode suggesting consistency in cloud optical properties (Fig. 5). This was confirmed by the visual sky observations at SFSU, where the average ϕ recorded when overcast LCF was observed was 0.96 and ϕ was greater than 0.85 during 86% of LCF observations. The low mode in Fig. 5 is suggestive of clear skies due to the very low degree of scattering. This mode had a significantly wider range, likely due to variations in atmospheric path length due to changes in solar elevation angle throughout the day and variations in concentrations of atmospheric aerosols such as dust, smoke, or air pollution.

Distinct differences existed between the relationships of τ and ϕ with solar elevation angle (β) under LCF compared with clear sky conditions (Fig. 6). From this, it is evident that a static threshold is less effective to distinguish LCF from clear sky conditions using τ because clear sky conditions at low solar elevation angles produce similar τ values to some LCF conditions at high solar elevation angles (Fig. 6a). However, since the difference between them scaled approximately linearly with solar elevation angle, a linear model for a solar elevation-dependent model was derived to provide a β-dependent threshold, whereby LCF is defined as $\tau < 0.0059\beta + 0.3$, and "clear skies" as $\tau > 0.0059\beta + 0.3$. The multiplier and offset were found using a model fit function that iteratively determined the match between LCF defined in this way and LCF defined using the $L\downarrow$ threshold technique, and selected the coefficients when the match was strongest (89.5% of periods). The majority of remaining periods, where LCF was defined as clear sky, occurred when β was less than 20°. Defining LCF conditions using ϕ was less accurate than using

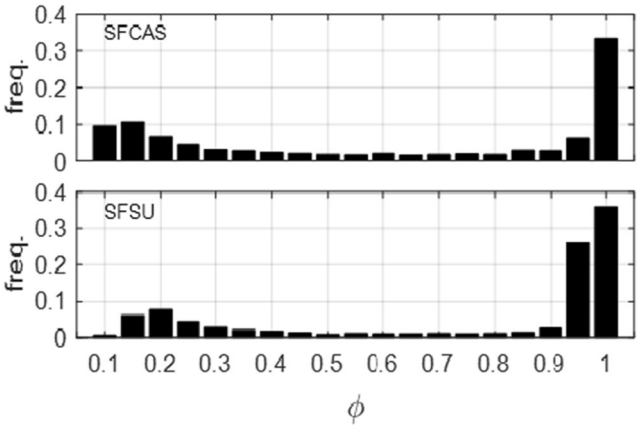

Fig. 5 Frequency distribution of the diffuse PAR fraction (ϕ) for two sites (SFCAS, SFSU) that directly measured PAR and PAR_D

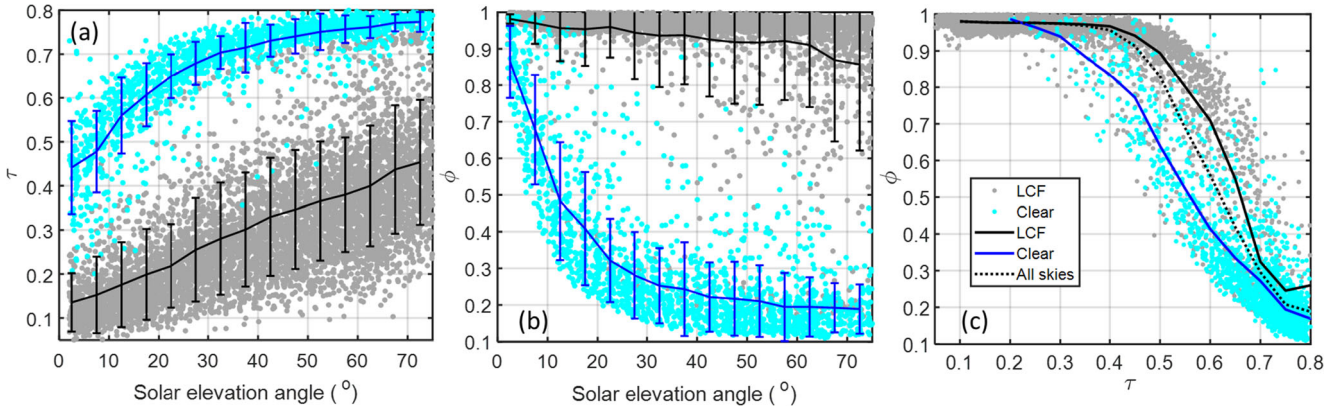

Fig. 6 Impact of solar elevation angle on **a** τ and **b** ϕ, and the relationship between ϕ and τ (**c**) for clear sky (cyan, $L\downarrow < 340$) and LCF periods (gray, $L\downarrow > 360$), with bin averages and standard deviation bars for clear sky (blue) and LCF (black) conditions

τ due to the convergence of values at low sun angles, when the long atmospheric path causes high degrees of scattering irrespective of sky condition (Fig. 6b).

The relationship between the two solar indices (Fig. 6c) was negative and non-linear and had a similar shape to that found for sites globally (Oliphant and Stoy 2018). There was a fairly consistent and high value of ϕ at low τ levels, mostly during LCF conditions along with some periods of clear sky conditions under low sun angles as shown in Fig. 6b. The bin average lines indicate a mean inflection point at approximately $\tau = 0.4$, above which ϕ declines somewhat linearly as τ increases, until a second inflection point at approximately $\tau = 0.75$, above which the lines straighten again (Fig. 6c). Both the clear sky and LCF conditions show a similar trend, although the upper inflection point is reached at much lower τ values under clear skies than that in LCF. This difference shows that LCF produces a higher amount of scattering relative to decrease of insolation at the surface compared with clear skies at low solar angles, except under very high and very low levels of scattering.

The general relationship depicted in Fig. 6c has been widely used to model ϕ, although with some discrepancy on the position of inflection points (e.g., Erbs et al. 1982; Weiss and Norman 1985; Roderick 1999; Gu et al. 1999). The basic form of the model is

$$\text{for } \tau < \tau_0 \; \phi = \phi_{0\text{ for }} \; \tau_0 < \tau < \tau_1 \phi = A_0 + A_1 \tau \text{ and for } \tau > \tau_1 \phi = \phi_1 \quad (7)$$

where the two inflection points are $[\phi_0,\tau_0]$ and $[\phi_1,\tau_1]$ and where

$$A_1 = \frac{\phi_1 - \phi_0}{\tau_1 - \tau_0} \text{ and } A_0 = \phi_1 - A_1 \tau_1 \quad (8)$$

Oliphant and Stoy (2018) not only used a global dataset to produce an optimal universal model, but also concluded that model coefficients (derived from the inflection points) varied regionally due to variations in cloud type and frequency as well as atmospheric aerosol sources and concentrations. To improve regional estimates, they presented a method for calculating the optimal inflection points using local measurements by selecting the values where the Nash and Sutcliffe (1970) model efficiency coefficient (*MEC*) was highest. Following this method, we used the two datasets that included both ϕ and τ observations (SFCAS, SFSU) to determine optimal model parameters for coastal California in summer for use in Eqs. 6 and 7 (Fig. 7). These were found by iteratively testing all of the combinations of τ_0, τ_1, ϕ_0, and ϕ_1 within plausible boundaries represented by the regions with colored contours in Fig. 7. The optimal inflection points for SFCAS were found to be [$\tau = 0.42$, $\tau_1 = 0.80$, $\phi_0 = 0.98$, $\phi_1 = 0.14$], which produced an MEC of 0.86 and for SFSU [$\tau_0 = 0.42$, $\tau_1 = 0.76$, $\phi_0 = 0.98$, $\phi_1 = 0.2$], which produced an MEC of 0.93. These coefficients are remarkably similar to one another and distinctly different from the global universal model (Oliphant and Stoy 2018) shown in Fig. 7, which produced *MEC* of 0.77 and 0.81 for SFCAS and SFSU, respectively.

3.4 Climatology of surface radiation components under different sky conditions

3.4.1 Frequency of sky conditions

Summer LCF frequencies determined by $L\downarrow > 360$ W m^{-2} averaged approximately 60% of hours among the four sites (Table 2). For both the San Francisco and Monterey Bay locations, the site closer to the coast had an approximately 10% higher frequency of LCF, and the San Francisco sites were higher in frequency than the Monterey Bay sites by about 10% on average. Both the higher LCF frequency in San Francisco than Monterey Bay and the reduction in frequency inland are trends observed from satellite-derived climatologies previously (e.g., Torregrosa et al. 2016). However, the exact frequency differences in the current study should be considered indicative only as these frequencies are subject to differences in the

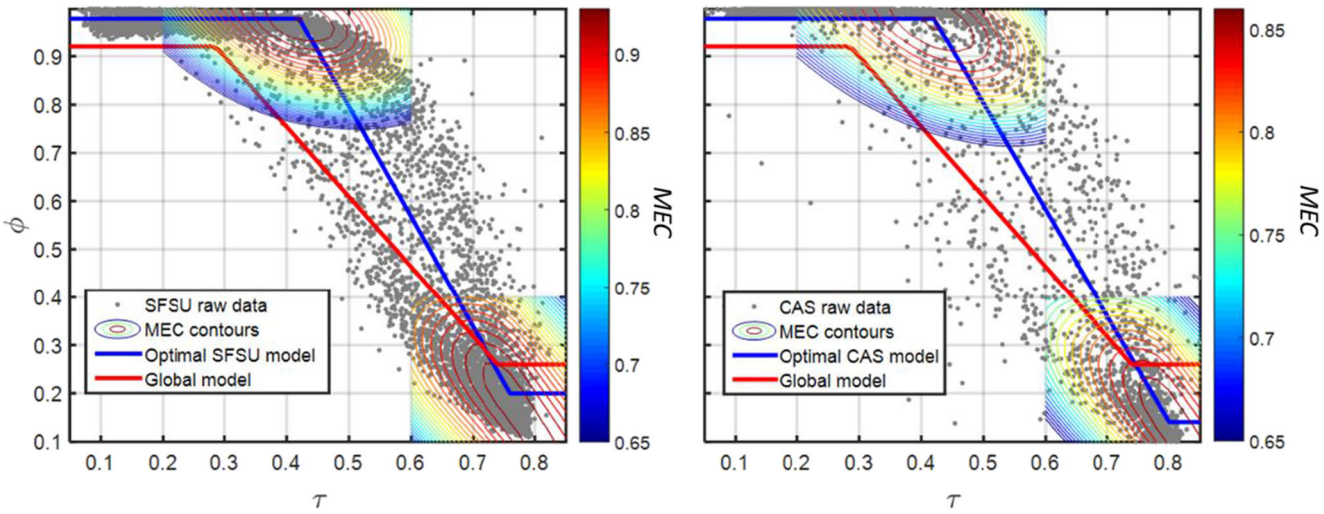

Fig. 7 Relationship between optical transmissivity (τ) and the diffuse fraction of PAR (ϕ) for **a** SFSU and **b** SFCAS datasets. Colored contour lines show magnitudes of the model efficiency coefficient (*MEC*, Nash and Sutcliffe 1970) for the two regions, which were used to determine the optimal model inflection points. The optimal ϕ model for these datasets is shown by the blue line (see text for model equation), and the global average model is shown by the red line (from Oliphant and Stoy 2018) for comparison

years in which they were observed. The majority of the remaining time was spent under clear sky conditions (33% on average), with only 7% of periods recording mixed sky conditions.Despite this, the frequencies of LCF occurrence are quite similar with a range of only 20%. The diurnal pattern of sky condition frequency was also quite similar among sites (Fig. 8). This was particularly the case at the time of highest LCF frequency, around 08:00 PDT, when all sites recorded nearly 80% LCF frequency. From this point in time, a general decline in LCF frequency occurred until mid- to late afternoon, and this was mirrored by a rise in clear sky frequency. Following the afternoon peak in clear skies, a general increase in LCF presence occurred at all sites until the morning peak at about 08:00 PDT. The largest differences in the diurnal pattern was higher frequencies of LCF occurring later into the afternoon at the two coastal sites and greater morning-to-afternoon differences occurring at the sites further inland. Mixed skies were observed at low levels throughout the day with a small increase occurring around mid-day during the peak of the transition between LCF and clear-sky periods.

Table 2 Frequency of observations during each study for different sky conditions determined using $L\downarrow$ thresholds, where LCF = $L\downarrow >$ 360 W m^{-2}, clear sky = $L\downarrow <$ 340 W m^{-2}, and mixed skies = 340 < $L\downarrow <$ 360 W m^{-2}

Frequency	SFCAS	SFSU	MBCF	MBFF
LCF	0.594	0.697	0.597	0.493
Clear skies	0.322	0.207	0.356	0.438
Mixed skies	0.084	0.096	0.047	0.069
n (30-min obs)	4528	12,425	3822	1817

3.4.2 Characteristic surface radiation magnitudes under different sky conditions

Summertime daily statistics from LCF and clear sky conditions determined using the $L\downarrow$ thresholds are compared for all four sites in Table 3, and diurnal patterns for SFCAS are presented in Fig. 9. This site was selected because it was the only site that both included direct measurements of PAR_D *and* was positioned over vegetation, allowing leaf temperature to be compared. However, all other sites showed very similar diurnal patterns. Daily total $K\downarrow$ was consistently about half the magnitude under LCF than clear sky conditions at 51.8% ± 3.8% (average ± standard deviation among the sites), with the largest difference in both daily total (48.9%) and maximum instantaneous values (403 W m^{-2}) occurring at SFSU (Table 3). The clearness index (τ) was similarly halved under LCF compared with clear sky periods when calculated from daily total radiation values, with the site average clear sky τ of 0.73 ± 0.02 and fog-impacted τ of 0.37 ± 0.03. The clearness index showed similar diurnal patterns under the two conditions, with lower values closer to sunrise and sunset due to lengthening atmospheric path, although this change was more dramatic in the case of clear sky conditions (Fig. 9e). PAR_G showed a very similar difference in magnitude to $K\downarrow$, and quite consistent differences in diffuse partitioning, with ϕ averaging 0.24 ± 0.02 under clear skies and 0.85 ± 0.06 during periods of LCF (Table 3). Similar to τ, the impact of atmospheric path length on ϕ is evident (Fig. 9f), with lower values occurring close to solar noon under both sky conditions, although, again, the solar angle impact was much larger under clear skies than fog. Despite quite different albedo observed among the four sites due to differences in surface color and

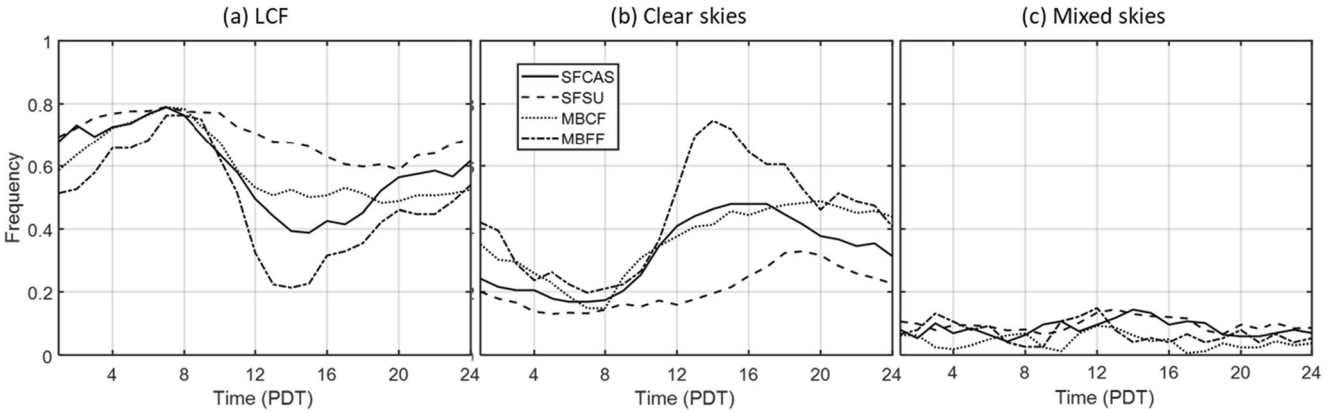

Fig. 8 Frequency of observations within each hour of the diurnal cycle for different sky conditions determined using $L\downarrow$ thresholds, where **a** LCF = $L\downarrow >$ 360 W m^{-2}, **b** clear skies = $L\downarrow <$ 340 W m^{-2}, and **c** mixed skies = 340 < $L\downarrow >$ 360 (W m^{-2})

structure, there was no significant change in daily albedo between LCF and clear sky conditions (Table 3), although increases in albedo during low solar elevation angles were evident under clear skies but not LCF conditions.

Daily total $L\downarrow$ averaged approximately 20 ± 2% higher under LCF than clear skies across all sites on a daily basis during summer (Table 3). There was no overlap at all found between values of $L\downarrow$ recorded under LCF compared with clear sky conditions, with quite similar differences throughout the diurnal cycle averaging 71 W m^{-2} (Fig. 9b). With narrower standard deviation error bars under LCF conditions despite the higher magnitude, $L\downarrow$ was also found to be more consistent under LCF than clear sky conditions throughout the 24-h period. This indicates the similarity of cloud base temperatures under meteorological conditions associated with LCF production, with more variations in clear sky conditions, which can include both onshore cool (but clear) marine air masses and offshore warm continental air masses. Despite the trade-off between increased $L\downarrow$ and decreased $K\downarrow$ under LCF conditions, the latter difference is greater in magnitude leading to an overall reduction in Q^*, especially during the day (Table 3; Fig. 9d). At night however, since $Q^* = L\downarrow - L\uparrow$ due to the absence of solar radiation, this pattern was reversed, and there was higher Q^* under LCF than clear skies (Fig. 9d). Due to

Table 3 Climatology of summertime radiation components and surface temperature on a daily basis under clear sky and LCF conditions at four locations in central coastal California, where daily values include mean summer daily total magnitudes and ratios of mean daily totals, "mean," "max," and "min" refer to mean summer daily mean and maximum and minimum values, respectively, and T_S refers to the surface temperature. All daily values were derived from 30-min ensemble averages defined as clear = $L\downarrow <$ 340 W m^{-2} and LCF = $L\downarrow >$ 360 W m^{-2}. Values denoted with * were modeled (see text for details)

Location		SFCAS living roof		SFSU campus roof		MBCF coastal farm		MBFF Inland airfield	
Component	Units	Clear	LCF	Clear	LCF	Clear	LCF	Clear	LCF
$K\downarrow$	MJ m^{-2}d^{-1}	29.2	13.2	28.2	13.8	28.3	14.7	28.2	16.1
$L\downarrow$	MJ m^{-2}d^{-1}	26.4	32.6	27.6	33.4	27.1	32.5	26.7	31.7
Q^*	MJ m^{-2}d^{-1}	15.9	10.4	13.4	9.0	14.9	10.1	17.9	12.1
PAR_G	mol m^{-2}d^{-1}	61.2	29.3	62.1	30.1	60.8	31.6	60.4	34.8
PAR_D	mol m^{-2}d^{-1}	14.0	27.0	14.6	25.8	16.5*	26.8*	13.8*	26.6*
PAR_S	mol m^{-2}d^{-1}	47.2	2.3	47.5	4.3	44.3*	4.8*	46.6*	8.2*
τ	ratio	0.749	0.340	0.728	0.355	0.698	0.375	0.726	0.414
ϕ	ratio	0.229	0.922	0.235	0.857	0.27*	0.85*	0.23*	0.77*
α	ratio	0.185	0.178	0.165	0.160	0.201	0.205	0.129	0.130
$K\downarrow$ max	W m^{-2}	988.7	572.4	947.7	544.4	980.0	625.0	982.7	670.3
Q^* max	W m^{-2}	654.0	419.6	589.3	387.1	667.4	456.3	760.3	545.7
Q^* min	W m^{-2}	−80.6	−10.0	−96.7	−19.7	−92.8	−11.1	−73.0	−11.5
T_S mean	°C	18.3	16.9	24.76	21.76	16.56	17.76	16.46	16.36
T_S min	°C	29.9	22.9	39.86	30.86	26.36	21.9	23.36	21.46
T_S max	°C	10.5	13.8	15.76	17.36	11.46	13.76	10.06	13.46

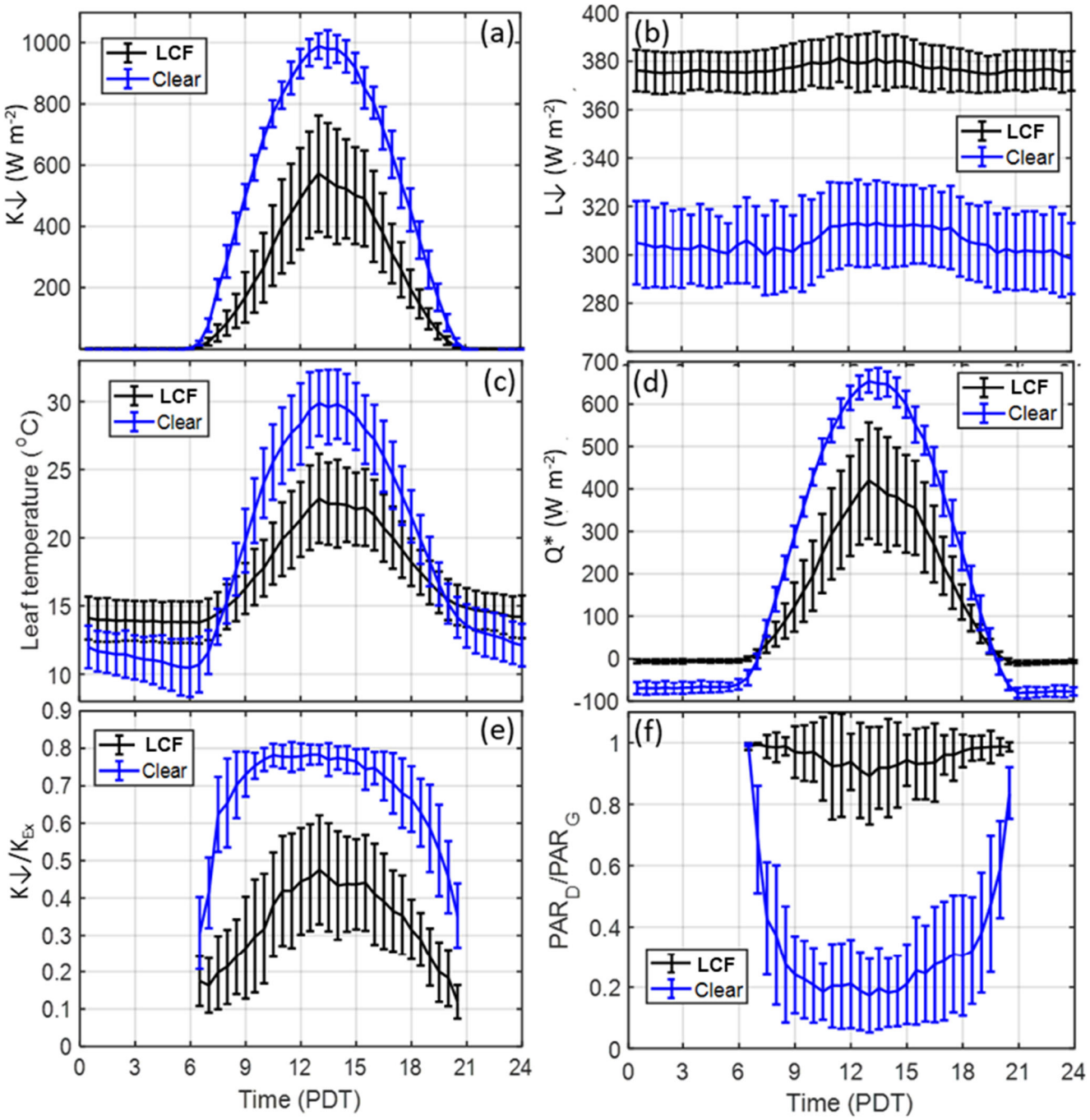

Fig. 9 Diurnal ensemble averages and standard deviations of (a) $L\downarrow$, (b) $L\downarrow$, (c) leaf temperature, (d) Q*, (e) τ and (f) ϕ, based on 30-min average radiationvalues for all periods defined as Clear $L\downarrow$=< 340 W m^{-2} and LCF = $L\downarrow$ > 360 W m^{-2} during summer observations from SFCAS

lower Q^* by day, the surface temperature was significantly lower during the day, with an across-site average in maximum temperature difference of 5.6 °C (Table 3). However, with the higher Q^* at night, this pattern was reversed when, by the hours before sunrise, the leaf temperature averaged 2.6 °C cooler under clear sky than LCF conditions (Table 3; Fig. 9c).

4 Discussion and conclusions

Advection fog processes produce frequent low cloud and fog conditions in coastal California during summer, particularly along the central and northern California coast. With a lack of convective or frontal clouds during this period, a distinctly

bimodal sky condition occurs: LCF or clear skies. The presence of LCF produces a consistent and distinctive impact on the surface radiation budget including large reductions (approximately half) in incident solar radiation reaching the surface (both full spectrum and PAR), large increases (approximately 180%) in diffuse beam PAR, consistent increases in down-welling longwave radiation (approximately 70 W m^{-2}), overall reductions in net radiation (although increases during the night), and moderated surface temperatures. These variations were found to be very consistent throughout the summer and among four sites located in San Francisco and Monterey Bay. In these locations, LCF conditions prevailed on average 60% of the time during summer with about 10% higher frequencies closer to the coast and about 10% higher frequencies in San Francisco than Monterey Bay. In all locations, LCF frequency peaked at 08:00 PDT (almost 80% of observations) and subsequently declined until mid- to late afternoon, with sites further from the coast declining more rapidly and having earlier minima LCF frequencies. All sites then steadily increased to maxima frequencies at 08:00 PDT.

The striking dissimilarity in radiation budget components between the two prevailing sky conditions means surface-mounted radiometers can be useful for monitoring LCF occurrence. Of the radiation components considered, $L\downarrow$ was determined to be the most accurate and useful for detecting LCF. For the temperature regime of coastal California in summer, we suggest that thresholds of LCF = $L\downarrow > 360$ W m^{-2} and clear sky = $L\downarrow < 340$ W m^{-2} should be used, with most values in between reflecting mixed sky conditions. However, a simple single threshold of 350 W m^{-2} could also be used without much reduction in accuracy. Errors associated with droplet deposition on the pyrgeometer (which recorded 3.6 W m^{-2} lower during events) is small compared with the departure between the typical values of $L\downarrow$ during fog (~375 W m^{-2}) and the 350 W m^{-2} threshold used to determine it. Therefore, very few samples would be likely to be misclassified due to deposition errors using this method. This method is likely to be useful in other locations with strongly bimodal sky conditions, although the thresholds will need to be adjusted where temperatures (and thus $L\downarrow$) differ significantly from central coastal California. The clearness index (τ) can also be effective for distinguishing between LCF and clear sky conditions, although it is only possible during daylight hours and has a lower accuracy than the $L\downarrow$ threshold method, especially at low solar elevation angles. The model derived for detecting LCF in this way for California is LCF = $\tau < 0.0059\beta + 0.3$ and clear-sky = $\tau > 0.0059\beta + 0.3$, where β is the solar elevation angle. Based on these analyses, it is recommended that deploying pyrgeometers could be a relatively low-cost, yet accurate and effective method to continuously monitor LCF presence at high temporal resolution.

Using previously developed methods, the partitioning of PAR into diffuse and direct beam components could be modeled using only observations of $K\downarrow$. However, in this study, we calculated unique model parameters optimized for use in coastal California during summer, which improved accuracy by about 10% compared with universal global model parameters provided previously by Oliphant and Stoy (2018). The revised model, based on the average of optimal model coefficients derived for two sites (SFCAS and SFSU) in this study, is as follows,

$$\begin{array}{l}\text{for } \tau < 0.42; \phi = 0.98, \text{for } 0.42 > \tau < 0.78; \phi = 1.925 + -2.25\tau \\ \text{and for } \tau > 0.78; \phi = 0.17\end{array} \quad (9)$$

It is also probable that this model is effective (preferable to the universal model) for use at other coastal locations dominated by LCF and clear sky conditions. However, the different relationships between τ and ϕ that were found under clear sky compared with LCF conditions (Fig. 6c) suggest that for mid-levels of τ, the model underestimates the fraction of diffuse light under LCF conditions and overestimates it under clear skies. It may be possible to refine these models further by separating LCF and clear sky conditions using the $L\downarrow$ threshold and applying separate models to the two populations.

The summer LCF regime has a consistent and strong impact on the surface radiation budget for ecosystems and agriculture located along the narrow coastal strip of central and northern California, and these are likely to have significant implications for plant functioning. Despite a lower availability of light for photosynthesis, the high proportion of diffuse beam PAR means the incident light is more isotropic in direction and therefore will better penetrate canopies enhancing light availability for leaves at lower levels in the canopy (Farquhar and Roderick 2003; Urban et al. 2007). Most ecosystem light use efficiency studies show that gross primary production saturates from moderate to high levels of PAR, meaning the reduction in magnitude of PAR_G is unlikely to have significant negative effect on photosynthesis. Furthermore, a number of previous studies have shown greater light use efficiency for diffuse beam than for direct beam PAR for a large number of ecosystems (e.g., Gu et al. 1999; Choudhury 2001; Alton 2008; Oliphant et al. 2011; Cheng et al. 2015; Williams et al. 2014; Hemes et al. 2020). A secondary effect of lower incident solar radiation is lower leaf temperature by up to 9 °C, reducing heat stress on upper leaves in the canopy. Although by day the increase in $L\downarrow$ is more than offset by the decrease in $K\downarrow$, at night, this additional energy under LCF conditions reduces nocturnal cooling, producing higher leaf temperatures by up to 3.5 °C and, in general, reducing the diurnal surface temperature range. The

impact on water stress is also likely to be significant with a third less available energy (Q^*) for evaporation and surface heating on a daily basis. This likely produces reductions in soil evaporation as well as transpiration due to cooler leaves and lower vapor pressure deficit driven by lower surface temperatures. Combined, we expect this to produce improvements in ecosystem water use efficiency. In general, the results of this study contribute to the characterization of microclimates of coastal ecosystems impacted by fog and low cloud, as well as methods to monitor fog presence.

Acknowledgments The authors are grateful to the California Academy of Sciences, San Francisco State University Department of Physics and Astronomy, managers of Jenson Farm, Watsonville, and the Naval Postgraduate School for permission to mount radiometers on their properties.

Code availability Not applicable, analyses routine and replicable from description in manuscript, or cited as described elsewhere.

Authors' contributions This study was conceived initially by Oliphant and Baguskas, and all three authors contributed to observational design, instrument deployment and maintenance, data management, and quality control. Most of the initial analysis and drafting of the manuscript was conducted by Oliphant. The manuscript and analysis were further honed by all authors, including in the revision stage, and all authors read and approved the final manuscript.

Funding NASA SBIR Phase II S1.08 (Oliphant) and USDA-NIFA USDA-NIFA Postdoctoral Fellowship (#2015-67012-22769) (Baguskas).

Data availability All data are freely available by directly contacting the corresponding author for files and metadata.

Compliance with ethical standards

Conflict of interest The authors declare that they have no conflict of interest.

References

Aida M (1977) Scattering of solar radiation as a function of cloud dimensions and orientation. J Quant Spectroscopy and Radiative Transfer 17:303–310. https://doi.org/10.1016/0022-4073(77)90109-1

Alton PB (2008) Reduced carbon sequestration in terrestrial ecosystems under overcast skies compared to clear skies. Agric For Meteor 148: 1641–1653

Baguskas SA, Peterson SH, Bookhagen B, Still CJ (2014) Evaluating spatial patterns of drought-induced tree mortality in a coastal California pine forest. For Ecol Manag 315:43–53. https://doi.org/10.1016/j.foreco.2013.12.020

Baguskas SA, Clemesha RES, Loik ME (2018) Coastal low cloudiness and fog enhance crop water use efficiency in a California agricultural system. Agric For Meteor 252:109–120. https://doi.org/10.1016/J.AGRFORMET.2018.01.015

Blonquist JM, Tanner BD, Bugbee B (2009) Evaluation of measurement accuracy and comparison of two new and three traditional net radiometers. Agric For Meteorol 149:1709–1721. https://doi.org/10.1016/j.agrformet.2009.05.015

Bradley SG, Gibson RG (1982) On the use of pyrgeometers in cloud. J. Appl Meteorol Clim 21(8):1155–1159

Brotzge JA, Duchon CE (2000) A field comparison among a domeless net radiometer, two 4-component radiometers and a domed net radiometer. Journal of Atmospheric and Ocean Technology 17:1569–1582

Carbone MS, Williams AP, Ambrose AR, Boot CM, Bradley ES, Dawson TE, Schaeffer SM, Schimel JP, Still CJ (2013) Cloud shading and fog drip influence the metabolism of a coastal pine ecosystem. Glob Change Biol 19:484–497. https://doi.org/10.1111/gcb.12054

Cheng SJ, Bohrer G, Steiner AL, Hollinger DY, Suyker A, Phillips RP, Nadelhoffer KJ (2015) Variations in the influence of diffuse light on gross primary productivity in temperate ecosystems. Agric. For. Meteor. 201:98–110. https://doi.org/10.1016/j.agrformet.2014.11.002

Choudhury BJ (2001) Estimating gross photosynthesis using satellite and ancillary data: approach and preliminary results. Remote Sens Environ 75:1–21. https://doi.org/10.1016/S0034-4257(00)00151-6

Chylek P, Ramaswamy V (1982) Simple approximation for infrared emissivity of water clouds. J Atmos Sci 39:171–177. https://doi.org/10.1175/1520-0469

Clemesha RES, Gershunov A, Iacobellis SF, Williams AP, Cayan DR (2016) The northward march of summer low cloudiness along the California coast. Geophys Res Lett 43:1287–1295. https://doi.org/10.1002/2015GL067081

Corbin JD, Thomsen MA, Dawson TE, D'Antonio CM (2005) Summer water use by California coastal prairie grasses: fog, drought, and community composition. Oecologia 145:511–521. https://doi.org/10.1007/s00442-005-0152-y

Dawson TE (1998) Fog in the California redwood forest: ecosystem inputs and use by plants. Oecologia 117:476–485

Emmel C, D'Odorico P, Revill PA, Hörtnagl L, Ammann C, Buchmann N, Eugster W (2020) Canopy photosynthesis of six major arable crops is enhanced under diffuse light due to canopy architecture. Glob Change iol 26:5164–5177. https://doi.org/10.1111/gcb.15226

Erbs DG, Klein SA, Duffie JA (1982) Estimation of the diffuse radiation fraction for hourly, daily and monthly-average global radiation. Sol Energy 28:293–302

Farquhar GD, Roderick ML (2003) Pinatubo, diffuse light, and the carbon cycle. Science 299:1997–1998. https://doi.org/10.1126/science.1080681

Fernandez DM, Torregrosa A, Weiss-Penzias PS, Zhang BJ, Sorensen D, Cohen RE, McKinley G, Kleingartner J, Oliphant AJ, Bowman M (2018) Fog water collection effectiveness: mesh Intercomparisons. Aerosol Air Qual Res 18:270–283. https://doi.org/10.4209/aaqr.2017.01.0040

Fischer DT, Still CJ, Williams AP (2009) Significance of summer fog and overcast for drought stress and ecological functioning of coastal California endemic plant species. J Biogeogr 36:783–799. https://doi.org/10.1111/j.1365-2699.2008.02025.x

Gu LH, Fuentes JD, Shugart HH, Staebler RM, Black TA (1999) Responses of net ecosystem exchanges of carbon dioxide to changes in cloudiness: results from two north American deciduous forests. J Geophys Res 104:31421–31434

Hemes KS, Verfaillie J, Baldocchi DD (2020) Wildfire-smoke aerosols lead to increased light use efficiency among agricultural and restored wetland land uses in California's Central Valley. J. Geophys. Res.: Biogeosciences:e2019JG005380

Hiatt C, Fernandez D, Potter C (2012) Measurements of fog water interception by shrubs on the California central coast. Atmospheric and Climate Sciences 2:525–531. https://doi.org/10.1007/s11852-016-0443-y

Iacobellis SF, Cayan DR (2013) The variability of California summertime marine stratus: Impacts on surface air temperatures. J Geophys Res Atmos 118:9105–9122. https://doi.org/10.1002/jgrd.50652

Jensen MP, Vogelmann AM, Collins WD, Zhang GJ, Luke EP (2008) Investigation of regional and seasonal variations in marine boundary layer cloud properties from MODIS observations. J Clim 21:4955–4973. https://doi.org/10.1175/2008jcli1974.1

Leipper DF (1994) Fog on the U.S. west coast: a review. Bull Amer Meteor Soc 75:229–240

Mooney HA, Arroyo MTK, Bond WJ, Canadell J, Hobbs RJ, Lavorel S, Neilson RP (2001) Mediterranean-climate ecosystems, in global biodiversity in a changing environment. Springer, New York, pp 157–199. https://doi.org/10.1007/978-1-4613-0157-8_9

Nash JE, Sutcliffe JV (1970) River flow forecasting through conceptual models part I—A discussion of principles. J Hydrol 10:282–290

Null EJ (1995) Climate of San Francisco. NOAA Technical Memorandum NWS WR-126

Oliphant AJ, Stoy PC (2018) An evaluation of semi-empirical models for partitioning photosynthetically active radiation into diffuse and direct beam components. J. Geophys. Res. Biogeosciences 123:889–901

Oliphant AJ, Spronken-Smith RA, Sturman AP (2003) Spatial variability of surface radiation fluxes in mountainous terrain. J Appl Meteorol 42:113–128

Oliphant AJ, Dragoni D, Deng B, Grimmond CSB, Schmid H-P, Scott SL (2011) The role of sky conditions on gross primary production in a mixed deciduous forest. Agric. For. Meteor. 151:781–779. https://doi.org/10.1016/j.agrformet.2011.01.005

Pilié RJ, Mack EJ, Rogers CW, Katz U, Kocmond WC (1979) The Formation of Marine Fog and the Development of Fog-Stratus Systems along the California Coast. J Appl Meteorol 18:1275–1286. https://doi.org/10.1175/1520-0450

Rastogi B, Williams AP, Fischer DT, Iacobellis SF, McEachern K, Carvalho L, Jones C, Baguskas SA, Still CJ (2016) Spatial and temporal patterns of cloud cover and fog inundation in coastal California: ecological implications. Earth Interact 20:1–19. https://doi.org/10.1175/EI-D-15-0033.1

Reindl DT, Beckman WA, Duffie JA (1990) Diffuse fraction correlations. Sol Energy 45:1–7

Roderick ML (1999) Estimating the diffuse component from daily and monthly measurements of global radiation. Agric For Meteorol 95:169–185

Rubio E, Caselles V, Badenas C (1997) Emissivity measurements of several soils and vegetation types in the 8–14, μm wave band: analysis of two field methods. Remote Sens Environ 59:490–521

Staley DO, Jurica GM (1972) Effective atmospheric emissivity under clear skies. J Appl Clim 11:349–356

Torregrosa A, Combs C, Peters J (2016) GOES-derived fog and low cloud indices for coastal north and Central California ecological analyses. Earth and Space Science 3:46–67. https://doi.org/10.1002/2015EA000119

Urban O, Janouš D, Acosta M, Czerný R, Marková I, Navrátil M, Pokorný R, Šprtová M, Zhang R, Špunda V, Grace J, Marek MV (2007) Ecophysiological controls over the net ecosystem exchange of mountain spruce stand. Comparison of the response in direct vs. diffuse solar radiation. Glob Chang Biol 13:157–168. https://doi.org/10.1111/j.1365-2486.2006.01265.x

Vasey MC, Loik ME, Parker VT (2012) Influence of summer marine fog and low cloud stratus on water relations of evergreen woody shrubs (*Arctostaphylos*: Ericaceae) in the chaparral of Central California. Oecologia 170:325–337. https://doi.org/10.1007/s00442-012-2321-0

Vasey MC, Parker T, Holl KD, Loik ME, Hiatt S (2014) Maritime climate influence on chaparral composition and diversity in the coast range of Central California. Ecology and Evolution 4:3662–3674

Weiss A, Norman JM (1985) Partitioning solar radiation into direct and diffuse, visible and near-infrared components. Agric. For. Meteor. 34:205–213

Weiss-Penzias P, Coale K, Heim W, Fernandez D, Oliphant AJ, Dodge C, Hoskins D, Farlin J, Moranville R, Olson A (2016) Total- and monomethyl-mercury and major ions in coastal California fog water: results from two years of sampling on land and at sea. Elem, Sci, Anth 4:00101. https://doi.org/10.12952/journal.elementa.000101

Whiteman CD, Allwine KJ (1986) Extraterrestrial solar radiation on inclined surfaces. Environ Softw 1:164–169

Williams AP, Still CJ, Fischer DT, Leavitt SW (2008) The influence of summertime fog and overcast clouds on the growth of a coastal Californian pine: a tree-ring study. Oecologia 156(2008):601–611. https://doi.org/10.1007/s00442-008-1025-y

Williams M, Rastetter EB, Van der Pol L, Shaver GR (2014) Arctic canopy photosynthetic efficiency enhanced under diffuse light, linked to a reduction in the fraction of the canopy in deep shade. New Phytol 202:1267–1276. https://doi.org/10.1111/nph.12750

Yang J, Wong MS, Menenti M, Nichol J (2015) Modeling the effective emissivity of the urban canopy using sky view factor. ISPRS J Photogramm Remote Sens 105:211–219. https://doi.org/10.1016/J.ISPRSJPRS.2015.04.006